Hydrodynamics Matters: Unravelling the Gas Transfer Law for the Energy Dissipation Process in a High-energy Stream

Zhipan Niu[1,2], Weiyang Zhao[1,2], Yihan Luo[1], Ademir Prata[3,4], and Hang Wang[2]

[1]Institute for Disaster Management and Reconstruction, Sichuan University, China.

[2]State Key Laboratory of Hydraulics and Mountain River Engineering, Sichuan University, China.

[3]Centro de Tecnologia, Federal University of Alagoas, UFAL, Maceió, Brazil.

[4]ARC Training Centre for the Transformation of Australia's Biosolids Resources, University of New South Wales, UNSW Sydney

Corresponding author: Weiyang Zhao (wyzhao_sl@163.com)

Key Points:

- Gas transfer in hydraulic jump is two orders greater than in estuaries and lowland rivers and comparable to rapids in whitewater rivers
- The primary pathway for gas transfer in highly agitated running flow involves free surface contact and bubble mediation
- A mechanistic model was developed by establishing the relationship between gas transfer and hydrodynamics

Abstract

Accurately quantifying air-water gas transfer is pivotal for understanding carbon cycles and assessing aquatic hypoxia prevalence. In the energy dissipation process of high-energy streams, gas transfer is extremely high, but the estimation becomes challenging due to the instantaneous variability in flow properties. Experiments in a laboratory open channel flume for a typical energy dissipation process (hydraulic jump) have been undertaken. The transfer efficiency E for the hydraulic jump lay between 0.037 to 0.162. These values are 4 to 7 times larger than those reported in previous studies with comparable layouts but different scales, highlighting the substantial impact of scale effects in bubble dynamics on gas transfer. Localized gas transfer velocities k_{600} exhibited a range from 340 to 985 m/day, falling within the order of 100 for estuaries and lowland rivers and comparable to rapids in a large whitewater river. Paired experiments were conducted to explicitly resolve the hydrodynamics of the free surface and bubbles. Subsequently, a mechanistic model was developed by establishing a relationship between gas transfer and hydrodynamics. The model physically clarified the gas transfer contribution from free-surface and bubble-mediated components and elucidated the reasons for gas transfer heterogeneity for different flows. The results provide insights into gas transfer estimation on a large scale.

Plain Language Summary

Understanding how gases exchange between air and water is crucial in environmental science. For instance, it enhances our comprehension of carbon cycles, which are pivotal in climate change research. Additionally, knowledge of the rate at which oxygen enters water aids in assessing water quality. In upstream fast flowing streams, such as those with intense turbulence, gas exchange occurs rapidly but can be challenging to measure due to the rapid fluctuations in flow properties and technical limitations. To address this, we conducted experiments in a laboratory flume, focusing on a common energy dissipation phenomenon known as a hydraulic jump. We identified a robust correlation between gas exchange and flow properties. Subsequently, we developed a model elucidating the mechanisms of gas exchange based on water flow dynamics and bubble behavior. This model effectively explains the variations in gas exchange under different conditions.

1 Introduction

Gas transfer is crucial within freshwater ecosystems, particularly when investigating carbon cycles or assessing the prevalence of aquatic hypoxia. It is estimated that streams and rivers annually release 650 Tg C (Lauerwald et al., 2015) and 1800 Tg C (Raymond et al., 2013) into the atmosphere, respectively, having an active role in global carbon evasions. Despite their significance, these fluxes are poorly understood, primarily due to inadequate quantification of gas transfer processes. On the other hand, recent studies reveal that 12.6% of rivers across 53 different countries have been identified as hypoxic, characterized by dissolved oxygen concentrations below 2 mg/L (Blaszczak et al., 2023). However, these findings have substantial uncertainty, partly attributable to limited knowledge regarding reoxygenation via gas transfer.

Gas transfer flux can be expressed as the multiplication of the gas transfer velocity (k_L) and the concentration difference between the air and water interfacial layers, in which the gas transfer velocity is typically the limiting component, since it presents large variations depending on different physical factors. While the process of gas transfer in still waters could be simply described by the direct effect of molecular diffusion, being generally a slow process, the presence of advection, enhanced turbulence and surface instability in running waters significantly augment the gas transfer velocity and makes its modeling much more complex. Gas transfer velocities are highly related to the flow regime. In a series of experimental flume studies, it was observed that gas transfer velocities in nonuniform flows passing submerged bricks were approximately 38% higher compared to those observed in smooth flow runs (Moog and Jirka, 1999a; b). Gas transfer velocities in supercritical flows were found to be 6-10 times greater than those in subcritical flows (Zhao et al., 2022). The overall gas transfer velocity becomes even more diverse (and normally larger) when entrained bubbles are present. Zhao et al. (2022) found the local transfer velocities at hydraulic jumps with local air entrainment exceed those in supercritical flows by a factor of up to three. The transfer velocities of headwater flows were estimated approximately 230-1200 times higher than those observed in ponds and lakes (Ulseth et al., 2019), and a remarkable 4000-fold variation was indicated between flat reaches with smooth flowing surfaces and steep rapids with broken surfaces in a large whitewater river (Hall et al., 2012).

In a natural scenario or under human intervention, certain areas in a river channel may have some spots of increased disturbance, like a sudden change in bed slopes or cross-sectional areas, bedform discontinuities such as cascades and step-pool geomorphology, and the presence of manmade hydraulic control such as a sluice gate. These features result in rapid energy dissipation and a flow regime transition from the supercritical flow to the subcritical flow, giving rise to a hydraulic jump (Henderson, 1966). An example of hydraulic jumps in a natural river channel is presented in Fig. 1. The intricate hydrodynamic characteristics of hydraulic jumps pose a significant challenge in predicting gas transfer accurately. More specifically, the instantaneously varying flow properties associated with hydraulic jumps may introduce temporal variability into the gas transfer velocity estimation. Moreover, the presence of the oscillating free surface in hydraulic jumps, along with the continuously entrained bubble clouds, add complexity to the quantification of gas transfer velocity. The hydraulic jump largely promotes the local gas transfer process and introduces a strong heterogeneity in gas transfer along the waterway. Limited understanding of gas transfer within hydraulic jumps has led to an underestimation of carbon evasion from headwater streams (Botter et al., 2022; Vautier et al., 2020). The imprecise characterization of its reoxygenation also hinders the evaluation of environmental risks for the hydraulic system (Chanson, 1995; Kamal et al., 2020)

In this study, we conducted a series of new experiments to investigate gas transfer within classical hydraulic jumps in a laboratory open channel flume. Through numerical simulations and advanced measurement techniques, we examined the air-water flow characteristics including surface turbulence and bubble clouds. This allowed us to explicitly resolve the surface and bubble dynamics. Leveraging coupled gas transfer experiments, we separated the free-surface transfer contribution and bubble-mediated contribution in this typical agitated flow and gained a clearer idea of gas transfer law in different regimes. Our study provides additional insights into the high heterogeneity of gas transfer velocities in rivers and streams, and also sheds light on a more precise gas transfer estimation on a large scale.

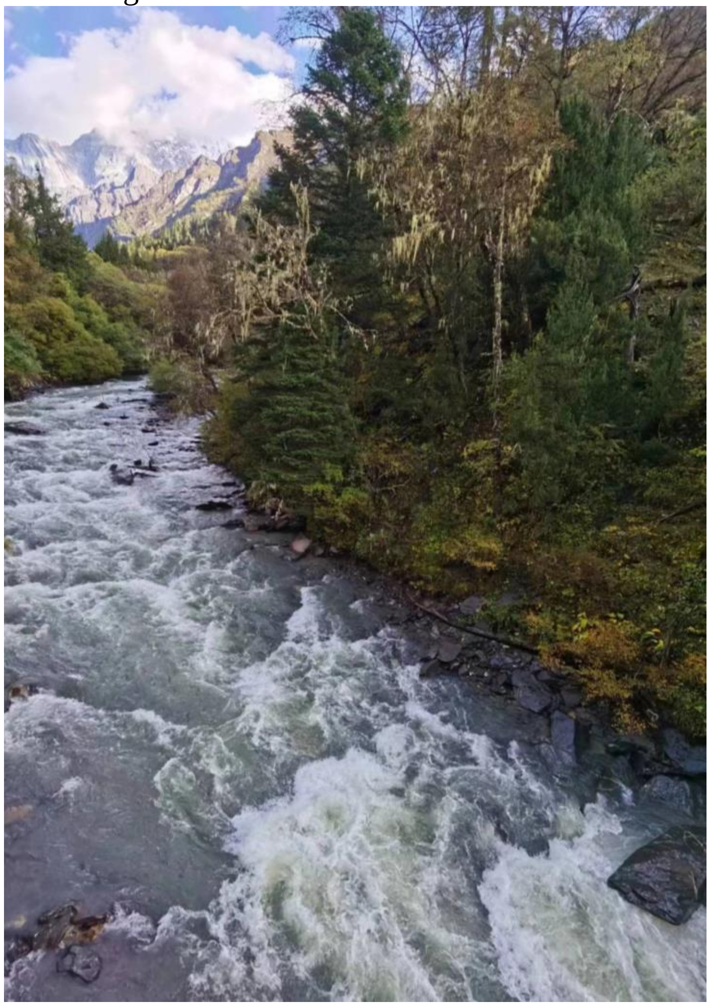

Fig. 1 Hydraulic jumps in a natural river channel (Xiaojin River, Sichuan Province, China)

2 Literature Review

2.1 Theoretical Frameworks for Gas Transfer

The liquid-side gas transfer velocity (k_L) is defined by the equation:

$$J = k_L (C_L - C_{L,i}) \quad (1)$$

where J is the liquid-gas mass flux (kg s^{-1} m^{-2}) of a dissolved substance, C_L and $C_{L,i}$ are the concentrations (kg m^{-3}) of that substance in the bulk liquid and immediately adjacent to the liquid-gas interface, respectively. For highly volatile gases such as oxygen, methane and carbon dioxide, $C_{L,i}$ can be approximated by the saturation concentration based on Henry's law.

Gas transfer has been investigated for more than a century, and several classic theoretical models were proposed to predict gas transfer velocity. Lewis and Whitman (1924) first proposed a two-film model, which presumed that two laminar sublayers ("films") respectively lie on each side of the interface, and inside the sublayers only molecular transport takes place, dramatically simplifying the problem. With the additional assumption of linear concentration distribution in the sublayers, the gas transfer velocity k_L was deduced from Fick's first law:

$$k_L = \frac{D_m}{h_w} \tag{2}$$

where h_w is the thickness of the liquid film, D_m is the gas molecular diffusivity in the liquid.

By the presence of turbulent sweeps, upwellings, downwellings, and vortices, fluid at the interfacial contacting area keeps being replaced by the turbulent motion of the liquid, and stable concentration distribution in the films cannot be reached in such a short time. Consequently, non-steady diffusion was considered, leading to the development of a penetration model. Higbie (1935) postulated a fixed duration for the exposure of interfaces and diffusion in films, and a new cycle of exposure and diffusion initiates after the completion of the preceding period. The time average gas transfer velocity was given by：

$$k_L = 2\sqrt{\frac{D_m}{\pi T}} \tag{3}$$

where T indicates the prescribed contacting time (s).

The penetration model first put forward the concept of "age" for the duration of contact of a parcel of "fresh" fluid (containing the studied substance) exposed to the surface. Adopting this concept, Danckwerts (1951) refined the model by replacing the fixed age (as considered by Higbie (1935)) by a statistical distribution of age. That is, the period of surface replacement for every parcel of freshwater at the surface has been modified from a fixed duration to a random distribution. The resulting surface renewal model was given by:

$$k_L = \sqrt{D_m S} \tag{4}$$

where S is the mean rate of renewal of the fresh surface (s^{-1}).

Rooting from the conception of surface renewal, models with more details of the flow field have been proposed. The large-eddy model hypothesizes that the large eddies sweep fresh liquid to the near-surface and then remove gas-enriched liquid back to the bulk water (Fortescue and Pearson, 1967). By presuming that the surface layer is divided into a series of rotational cells with diameter L and velocity proportional to the root mean square (RMS) value of turbulent velocity u', the surface renewal frequency S is proportional to u'/L. The large-eddy model yields:

$$k_L^+ = \frac{k_L}{u'} \propto Sc^{-\frac{1}{2}} Re_t^{-\frac{1}{2}} \tag{5}$$

where k_L^+ denotes dimensionless gas transfer velocity, Sc is Schmidt number ($Sc = D_m / \nu$), $Re_t = u'L/\nu$, is turbulent Reynold number, ν is the kinematic viscosity ($m^2\ s^{-1}$).

Drawing from observations of the tendency of surface damping to frequently filter large-scale motions in proximity to the surface, Lamont and Scott (1970) proposed the small-eddy model, which posits that the small eddies contribute to the surface renewal. Assuming that the surface renewal frequency S is controlled by Kolmogorov-scale eddies encompassing both the inertial motions and the viscous motions, $S \propto (\varepsilon/\nu)^{1/2}$, and ε is the surface dissipation rate of the turbulent kinetic energy ($m^2\ s^{-3}$). K_L^+ could be given as

$$k_L^+ = \frac{k_L}{u'} \propto Sc^{-\frac{1}{2}} Re_t^{-\frac{1}{4}} \tag{6}$$

The gas transfer velocity derived from the surface renewal model highly depends on the residence time of the surface renewal eddies or the frequency of surface renewal. However, the definition of surface renewal is ambiguous in different works, and almost none are directly related to the near-interface situation (Tamburrino and Gulliver, 2002).

A surface divergence model was put forward to better connect with the surface turbulence. Realizing especially in unsheared interfaces with high Schmidt number Sc, there is a sublayer even thinner than the viscous layer and eddies' length scale, where important fluid motions are all confined, and the flow motions in the sublayer are expressed by a single parameter, the surface divergence strength β. Chan and Scriven (1970) were the first to try to connect the surface divergence strength to the gas transfer velocity. Later, relying on numerical simulation, McCready et al. (1986) proposed that:

$$k_L \propto Sc^{-\frac{1}{2}} (\overline{\beta^2})^{\frac{1}{4}} \tag{7}$$

where $\overline{\beta^2}$ is the mean-square surface divergence.

2.2 Gas Transfer in Hydraulic Jumps

A hydraulic jump occurs when a high-velocity (supercritical) open-channel flow runs into a low-velocity (subcritical) region with an abrupt rise in flow depth. With complex two-phase flow characteristics including a very turbulent rolling surface and entrapment and entrainment of bubble clouds, gas transfer in hydraulic jumps is highly enhanced and could not be easily described by any of the theoretical models.

In engineering applications, gas transfer efficiency E has been usually adopted to characterize the gas transfer performance (Gulliver et al., 1998):

$$E = \frac{C_d - C_u}{C_s - C_u} \tag{8}$$

where C_u and C_d are the gas concentrations at the upstream and downstream ends, respectively. C_s is saturated dissolved gas concentration. E has a range between 0, for no gas transfer, and 1, for total downstream saturation. A series of empirical equations were proposed to predict E based on data fitting, and Table 1 summarizes the ones in flume experiments. Since none of them explains the gas transfer mechanism, the equations are case-specific and cannot be simplistically extrapolated to a broader range.

197 **Table 1** Relevant experimental flume studies of gas transfer in hydraulic jumps

Reference	Equation	Hydraulic parameter			
		Fr_1 (-)	Q (L/s)	Re (-) × 10^4	W (m)
Holler (1971)	$E_{20} = 1 - 1/(1 + 0.0463\Delta U^2)$	-	-	-	-
Apted and Novak (1973)	$E_{15} = 1 - 1/10^{0.24\Delta H}$	1.9-8	4	4	0.1
Avery and Novak (1975)	$E_{15} = 1 - 1/(1 + 0.23(q/0.0345)^{3.4}(\Delta H/d_1)^{4.5})$	2-9	1.45-7.1	1.45-7	0.1
Avery and Novak (1978)	$E_{15} = 1 - 1/(1 + 1.0043 \times 10^{-6} {Fr_1}^{2.1} Re^{0.75})$	2-9	1.45-7.1	1.45-7	0.1
Wilhelms et al. (1981)	$E_{15} = 1 - 1/(1 + 4.924 \times 10^{-8} {Fr_1}^{2.106} Re^{1.034})$	1.9-9.9	9.2-26.3	2.4-4.3	0.38
Kucukali and Cokgor (2006)	$E_{20} = 0.77\Delta H^{0.73} q^{0.24}$	2.2-6.4	7-26	1.4-5.4	0.5
Zhao et al. (2022)	$*E_{20} = 0.0426 E_L/H_1$	2.2-5.5	2.78-5.77	4.0-8.3	0.25

Note: ΔU = difference in flow velocity; ΔH = Difference in flow depth; Fr_1 = inflow Froude number; Re = Reynolds number; q = discharge per unit width; E_L = energy loss; H_1 = total head at upstream conjugate depth; E_{20} = gas transfer efficiency at 20 °C; E_{15} = gas transfer efficiency at 15°C. *denotes that the equation was fitted in the present study based on the corresponding literature data.

3 Experiments and Instrumentation

3.1 Experimental Facility and Flow Conditions

Experiments were conducted in a recirculation system with a 6.8 m long, 0.4 m wide and 0.5 m deep horizontal rectangular channel built with glass bottom and sidewalls. At the upstream end, a header tank with a vertically converging rectangular nozzle provided supercritical inflows. The nozzle had an adjustable opening, and the bottom plate of the nozzle was aligned with the channel bed. A tail tank measuring 2.0 × 1.3 × 1.8 m^3 was configured to facilitate a seamless outflow with minimal head loss and turbulence. Within the tail tank, sparging systems and mixing systems were installed, and one submersible pump with a maximum discharge of 25 L/s circulated water to the upstream header tank. The flow rate was controlled by a water valve and measured by an electromagnetic flowmeter with a precision of ± 1%. The nitrogen sparging system employed to eliminate oxygen from the recirculation system consisted of a carefully arranged array of air diffusers. These diffusers were evenly spaced at 5 cm intervals across the bottom of the tail tank. The mixing system consisted of two smaller submersible pumps (each with a maximum discharge of 3.6 L/s) at the tank corners, with the outlets positioned diagonally. Most of the free surface of the flow in the flume was covered by plastic membranes (bubble wrap), and the water surfaces in the header and tail tanks were covered with foam boards. These covers were used to prevent unconsidered oxygen from entering the recirculation system. Fig. 2 illustrates the experimental facility.

In the horizontal channel, a Cartesian coordinate system can be adopted for referencing positions, with x designating the longitudinal distance from the start of the horizontal flume and y signifying the vertical distance from the channel bed. Different hydraulic jumps were generated in the flume by adjusting the nozzle opening height from 1.6 cm to 2.6 cm and discharge from 15.0 L/s to 18.6 L/s, with $2.63 < Fr_1 < 6.03$ ($Fr_1 = U_1/\sqrt{gd_1}$) and $1.32 \times 10^5 < Re < 1.67 \times 10^5$ ($Re = 4U_1R_h/\nu$, with R_h the hydraulic radius) (Table 2). The mean jump toe positions x_t were controlled at $x = 5.0 \pm 2.5$ cm by a vertical undershoot sluice gate at the end of the channel. The supercritical flow length sufficiently avoided the interaction between the jump toe and the nozzle, while preventing excessive reaeration that would otherwise arise from extensive supercritical flow surface areas within the system, so that all significant gas transfer took place within the section of the hydraulic jump roller.

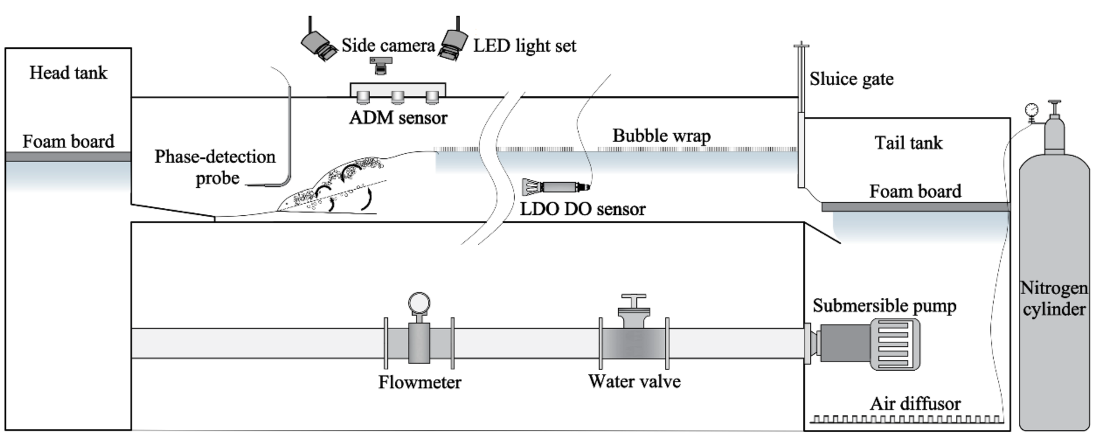

Fig. 2 Experimental setup and typical hydraulic jump

Table 2 Summary of hydraulic conditions and gas transfer velocity.

Case	Q (L/s)	d_1 (cm)	U_1 (m/s)	Fr_1 (-)	Re (-)× 10^5	L_j (cm)	d_2 (cm)	$k_{L,20}$ (m/day)	*k_{600} (m/day)	K_2^j (1/day)	$E_{e,20}$ (-)
1	17.5	1.75	2.50	6.03	1.61	66.5	14.6	1096.8	984.6	11967.3	0.162
2	15.2	1.68	2.26	5.57	1.40	60.5	11.6	790.1	709.3	9197.5	0.124
3	18.6	2.19	2.12	4.58	1.67	61.5	13.3	718.0	644.6	9432.6	0.087
4	15.8	2.22	1.78	3.81	1.42	51.5	10.7	500.4	449.2	6972.0	0.063
5	18.6	2.92	1.59	2.98	1.62	46.5	10.8	476.2	427.5	7173.2	0.045
6	15.0	2.75	1.36	2.63	1.32	41.5	9.0	379.2	340.5	6436.3	0.037

*k_{600} was calculated based on Equation 24 in the paper. Simple scaling law by the ratio of the Schmidt numbers should be used with caution among gases with different solubilities.

3.2 Experimental Procedure

For each flow condition, a duo of experiments was undertaken: one to assess gas transfer and the other to characterize hydrodynamics. Prior to commencing the gas transfer experiment, fresh tap water was injected into the recirculation system, and the dissolved oxygen content was systematically eliminated through continuous bubbling of nitrogen gas in the tail tank. Meanwhile, two mixing pumps and one transfer pump were operated to guarantee a homogeneous distribution of dissolved oxygen throughout the entire system. The whole sparging process persisted for approximately 30 min, until the dissolved oxygen (DO) concentrations measured in both the header and tail tank decreased from saturation to 2.0 mg/L. At that point, the sparging system was deactivated, followed by a 5-minute interlude to expel any lingering nitrogen bubbles in the system. The hydraulic jump was then created in the flume by operating the submersible pump and adjusting the water valve. A plastic membrane, with its smooth side in contact with the water, was placed over the water surface in the flume, leaving only the hydraulic jump exposed to the ambient air (for further details, refer to Zhao et al. (2022), who utilized a similar setup). The positions of the jump toe were adjusted to the same location, and the DO concentration sensor was positioned 1.0 m before the exit, 5 cm above the flume bed to record the DO increase with time. Each test lasted 5400 s to capture a whole picture of the gas transfer process, and the water temperature variations for all experiments were within 2°C.

Following the gas transfer experiments, hydrodynamics measurements for the identical flow conditions were executed. To ensure consistent water temperature, a portion of the water in the tank was replaced with fresh tap water prior to each experiment. Additionally, plastic membrane and foam boards were positioned the same way as in the gas transfer experiment to ensure identical hydraulic jumps. Acoustic displacement meters (ADMs) and a dual-tip conductivity phase-detection probe were used to detect the free surface and bubble dynamics.

3.3 Instrumentation and Data Processing

The instantaneous water surface elevations were measured non-intrusively by ADMs (Microsonic Mic+25/IU/TC, Dortmund, Germany). Six ADMs were aligned to and moved along the channel centerline, all calibrated onsite and scanned at 100 Hz for 240 s, covering a longitudinal distance of x = 0.05 to 1.00 m with a spacing of 0.05 m between two nearby ADMs. For each ADM sensor, the maximum detection distance is 0.35 m from the sensor head, with a measurement error of less than 0.18 mm. The response time of each sensor is 32 ms with a sampling rate of 100 Hz. Fig. 3 shows an example of a sample count distribution. All ADM sample data were post-processed in RStudio (R version 4.2.1 (R. Core Team, 2022)) with an in-house code using robust outlier cutoff filtering approach (Valero, 2018). The technique guarantees reasonably stable mean water elevation and fluctuation magnitude results.

The entrained air bubbles were detected intrusively using a dual-tip conductivity phase-detection probe. The probe was manufactured at Sichuan University, with an identical design to those used by Zhao et al. (2024). The probe's two-needle sensors, each with a concentric stainless-steel outer electrode (Ø = 0.8 mm) and an internal platinum electrode (Ø = 0.1 mm), are parallelly oriented along the main flow direction, with a longitudinal separation distance of 6.5 mm between the leading and trailing sensor tips. At each measurement site, both sensors were scanned at 20 kHz for 60 s. The air concentration and bubble counts are provided by the binarized leading tip signal (0 for water and 1 for air phase, an example is illustrated in Fig. 4), and the time-averaged interfacial velocity is calculated using a cross-correlation between the raw signals of the two tips (Chanson and Toombes, 2002). The probe's elevation was measured using a Vernier caliper installed on a trolley's supporting arm, with a precision of 0.1 mm.

The DO concentration was measured by a portable multiparameter meter (Hach HQ 2200, USA) with a field luminescent oxygen sensor (Hach Intellical LDO101, USA). The DO concentrations were sampled every 10 s for at least 5400 s. Typical raw signals are shown in Fig. 5. A Hampel filter was applied using (2 × 15 + 1) window length and Ron Pearson’s 3 sigma edit rule (Pearson, 1999). Since the raw DO concentration presents a very smooth change with time, the filtering only slightly smooths the signal (Fig. 5). Afterward, the gas transfer was calculated based on the filtered DO time series.

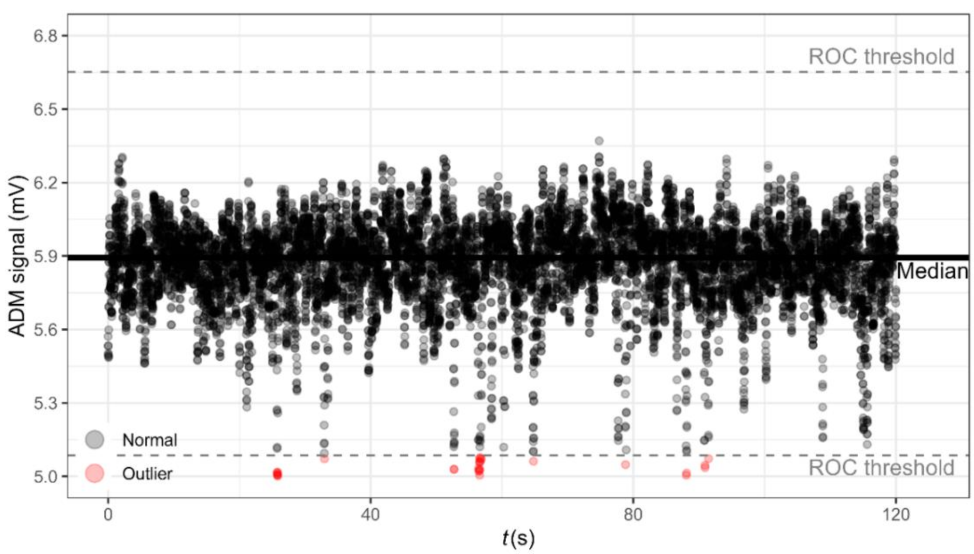

Fig. 3 Example of a sample count distribution and robust outlier cutoff (ROC) filtering approach of the ADM signals

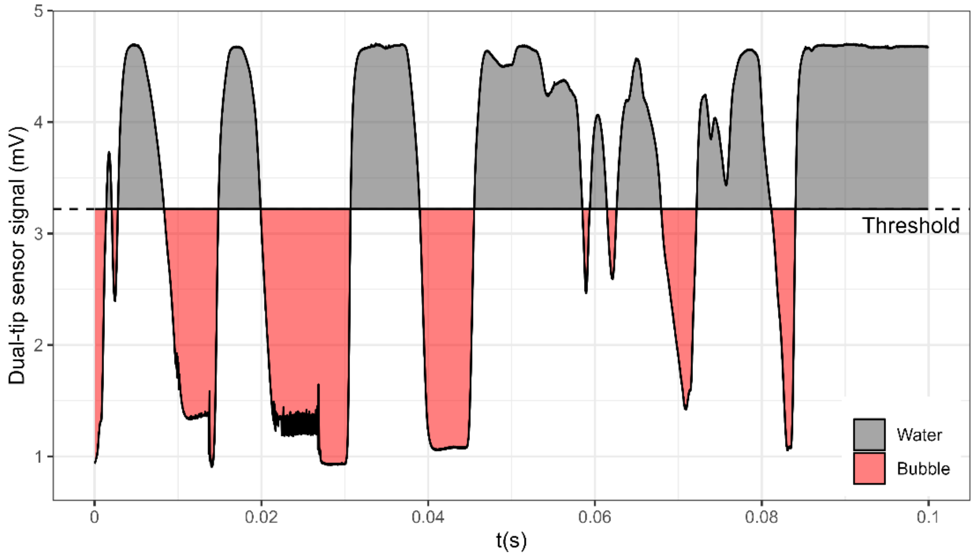

Fig. 4 Example of the raw data and separation of air bubbles and water of the dual-tip sensor signals

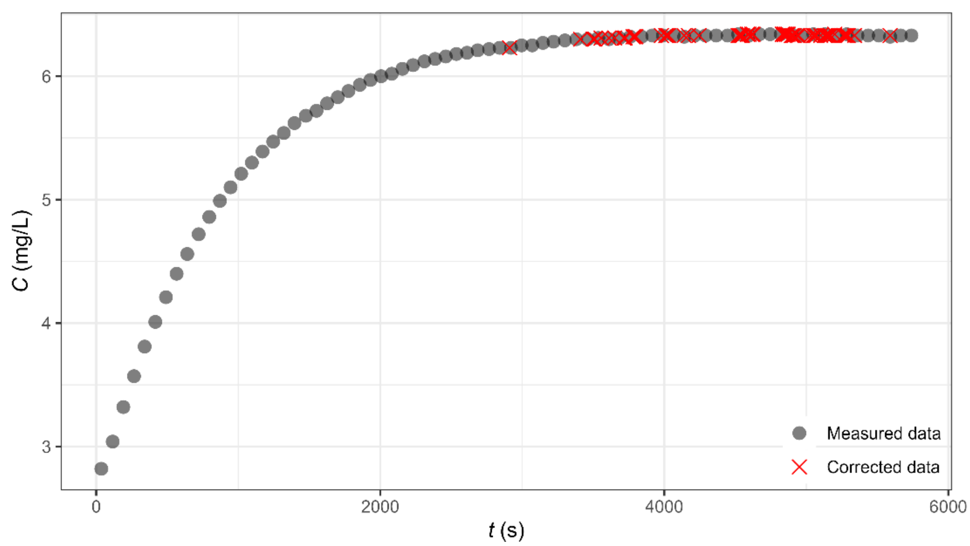

Fig. 5 Example of a continuous DO concentration measurement and Hampel filtering approach of DO samples

4. Gas Transfer of Hydraulic Jumps

4.1 Gas Transfer Efficiency

The gas transfer process in hydraulic jumps was studied by measuring oxygen levels using the procedure detailed in section 3. We collected time series data for instantaneous oxygen concentrations (C) for various cases of hydraulic jumps where $2.5 < Fr_1 < 6.5$. Fig. 6 exhibits the progression of DO saturation percentage within the recirculation system. The concentration of oxygen in hydraulic jumps with smaller inflow Froude numbers (Fr_1) increased steadily and at a moderate rate over time. Conversely, in cases with larger Fr_1, the concentration initially rose rapidly but gradually plateaued due to the constraint of a saturation concentration limit.

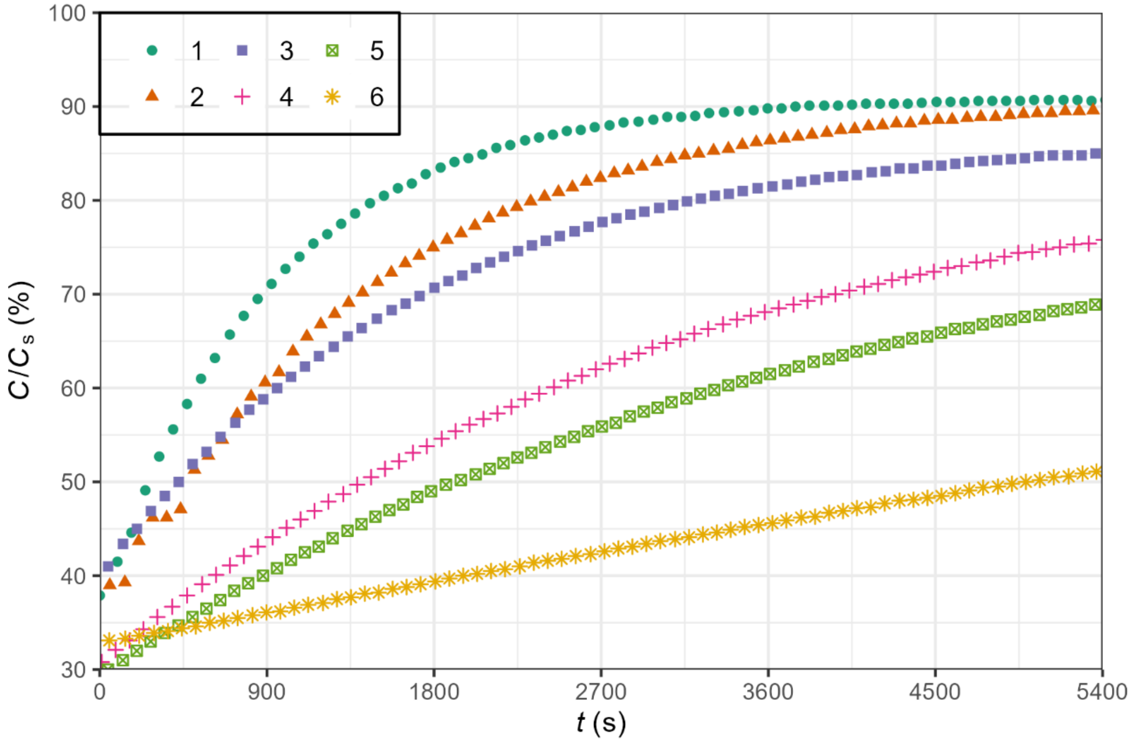

Fig. 6 Reaeration processes for different hydraulic jumps. Legend indicates the cases, as in Table 2 (note: only every 2nd data point is shown for better legibility)

The volumetric transfer coefficients for the whole system K_{vol} were obtained based on a nonlinear regression analysis with the filtered DO concentration time series following an exponential function given by (Bung and Valero, 2018)

$$C(t) = C_S - (C_S - C_0) \times e^{(-K_{vol} t)} \quad (9)$$

where C_0 is the initial concentration. To make a better comparison with the previous studies the gas transfer efficiency E was calculated. The calculation method is referred to Appendix A.

The gas transfer efficiency in the present study was compared with previous laboratory data. Following a similar trend, the transfer efficiencies in the present study were also found to increase with increasing energy dissipation efficiency, which was calculated as the ratio of the energy loss along the hydraulic jump (E_L) relative to the upstream total water head (H_1). The comparison is illustrated in Fig. 7. Transfer efficiencies exhibit significant variability across different studies, which can be attributed to various factors. One factor is the methodology employed to determine the transfer efficiency. May of the previous studies sampled the concentration at both upstream and downstream locations of the hydraulic jump and determined the transfer efficiency by analyzing variations along the hydraulic jump (Kucukali and Cokgor, 2020; Wilhelms et al., 1981). However, for indoor channel experiments, the concentration difference over such a brief distance is typically small and might be significantly affected by measurement errors. Additionally, the intrusion of the probe into the upstream supercritical flow strongly disturbs the flow field, introducing uncertainties to the quantification of gas transfer. Another potential source of variability stems from the method employed for dissolved oxygen (DO) measurement. Specifically, when employing the gas tracer method, the proportional relationship between the trace substance and the rate of oxygen transfer within bubbly flows may become invalid (Bennett and Rathbun, 1971). Furthermore, variations in the estimation of travel time through the hydraulic jump can also contribute to disparities in transfer efficiency.

In the present study, we adopted a methodology similar to that utilized by Zhao et al. (2022). This approach allowed for the evaluation of transfer efficiencies under comparable inflow Froude numbers (Fr_1) within the range of 2.6 to 6.0. Notably, our findings reveal a significant difference when compared to previous research, as the values obtained in our study were much higher, by a factor of 4 to 7 (Fig. 8a). The Reynolds numbers in our investigation fell within the range of 1.3×10^5 to 1.7×10^5, whereas the previous study reported values between 4.0×10^4 and 8.3×10^4 (Fig. 8b). These variations may be primarily attributed to the scale effects observed in hydraulic jumps. Further supporting evidence for the positive correlation between Reynolds number and transfer efficiency includes: (1) The Reynolds number from Wilhelms et al. (1981)'s data falls within the range of 1.4×10^5 to 1.6×10^5, and the transfer efficiencies align more closely with our present study, surpassing the data from Zhao et al. (2022); (2) Analyzing separately two groups of data from Kucukali and Cokgor (2020), one with a Froude number around 4, where an increase in Reynolds number from 7.6×10^4 to 1.9×10^5, results in a transfer efficiency rise from 0.033 to 0.071, and another group with a Froude number around 5, showing an increase in Reynolds number from 9.5×10^4 to 1.7×10^5 leads to a transfer efficiency increase from 0.057 to 0.093.

Wang & Chanson (2016) explored cases with Reynolds numbers between 2.1×10^4 and 1.6×10^5, indicating roller surface dynamics and bubble dynamics are scale-sensitive. Particularly, as the Reynolds number increases, the frequency of roller surface oscillation tends to rise. Moreover, higher Reynolds numbers lead to enhanced turbulent shear forces, resulting in the breakup of larger bubbles, and a marked increase in the interfacial area. This effect can be observed in Fig 9, which presents the side-view photos of the hydraulic jumps from both the present study and Zhao et al. (2022) with similar Froude numbers.

Considering that roller surfaces and entrained bubbles act as two major paths for gas transfer of hydraulic jumps, the change in interfacial layer turbulent intensity and water-atmosphere/ -bubble contacting area with varying Reynolds numbers provide a significant explanation for the observed increase in transfer efficiency. These results suggest the necessity of developing a mechanistic gas transfer model that carefully examines the surface and bubble dynamics for flux estimation in prototype and natural conditions.

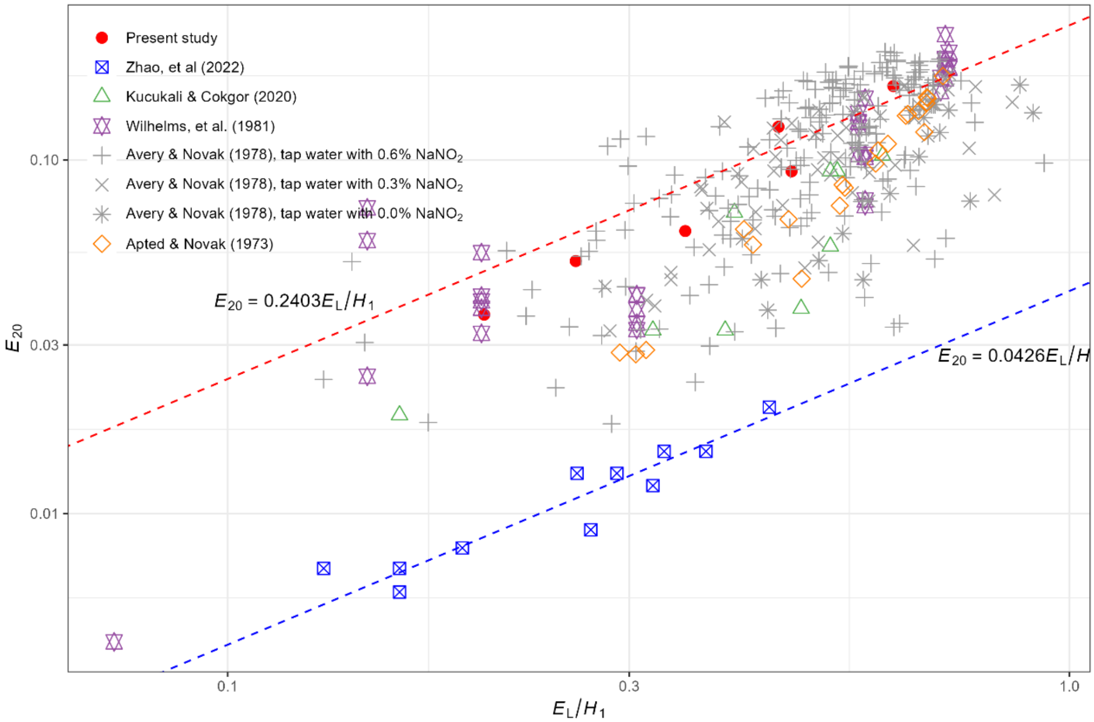

Fig. 7 Hydraulic jump transfer efficiency normalized to 20°C (E_{20}) as a function of energy loss along the hydraulic jump (E_L) relative to the upstream total water head (H_1). [Comparison of present data with that of Apted and Novak (1973), Avery and Novak (1978), Wilhelms et al. (1981), Kucukali and Cokgor (2020), Zhao et al. (2022).

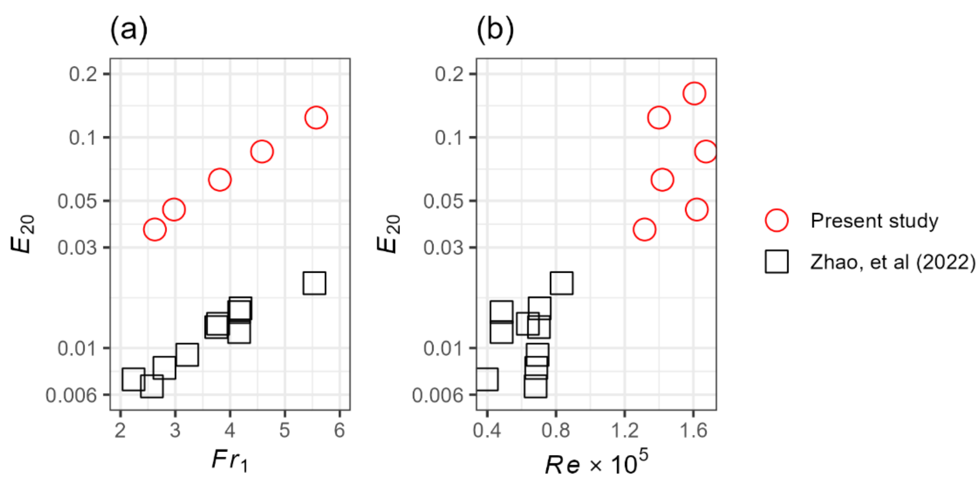

Fig. 8 Comparison of present hydraulic jump transfer efficiency (E_{20}) with a previous study (Zhao et al. (2022)) in terms of (a) inflow Froude number (Fr_1); (b) Reynolds number (Re)

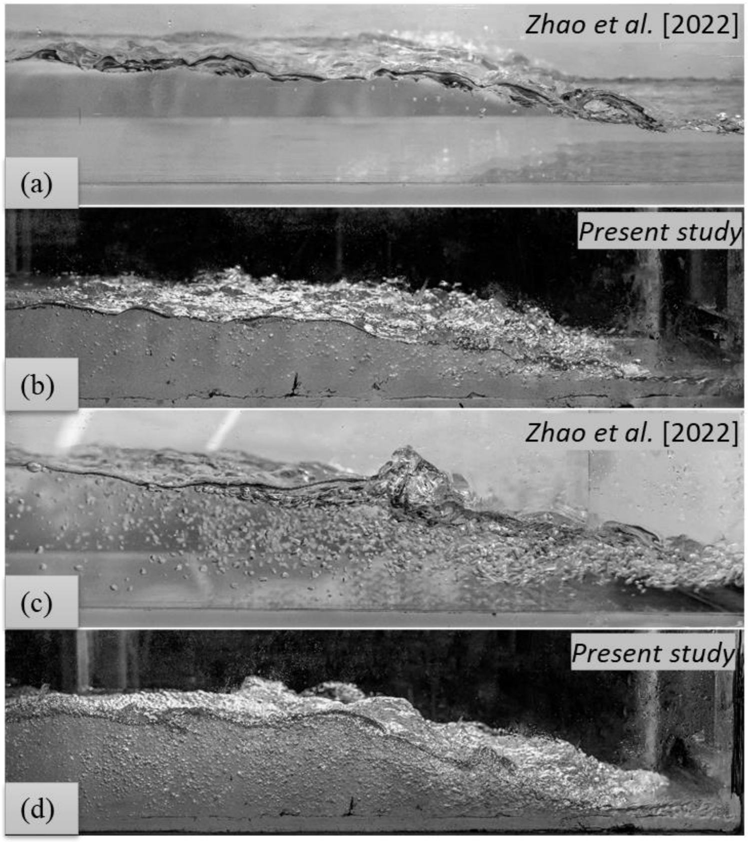

Fig. 9 Side-view of the hydraulic jump for (a) Zhao et al. (2022), q = 4.44 L/s, Fr_1 = 2.50, Re = 6.8 × 10^4; (b) present study, q = 15.0 L/s, Fr_1 = 2.63, Re = 1.3 × 10^5; (c) Zhao et al. (2022), q = 5.77 L/s, Fr_1 = 5.54, Re = 8.3 × 10^4; (b) present study, q = 15.2 L/s, Fr_1 = 5.57, Re = 1.4 × 10^5

4.2 Mechanistic Gas Transfer Model

The hydraulic jump displays intricate characteristics in terms of two-phase flow, encompassing strong free-surface dynamics, internal turbulence development and air entrainment evolution. Previous studies utilized an overall gas transfer velocity to represent the gas transfer rate, identifying distinct gas transfer regimes during bubble entrainment (Hall et al., 2012; Ulseth et al., 2019). However, the overall gas transfer velocity lacks a detailed description of the interaction between bubbles and air, resulting in an imprecise characterization of the bubble-mediated contributions to the gas transfer process. In order to improve the quantification of the gas transfer process, a mechanistic model was developed, explicitly considering free surface and bubble-mediated exchange. The volumetric transfer coefficient K_2^j (s^{-1}) is introduced to characterize the gas transfer rate within the hydraulic jump. This metric can be further decomposed into two distinct contributions: free surface transfer coefficient $(k_\mathrm{L}a)_\mathrm{s}$ and bubble-mediated transfer coefficient $(k_\mathrm{L}a)_\mathrm{b}$ (further details refer to Appendix B):

$$K_2^j = (k_L a)_s + (k_L a)_b \tag{10}$$

Free Surface Pathway Contribution

The free surface contribution is driven by diffusive mass transfer, which is enhanced by turbulence and active interfacial area. The free surface gas transfer velocity $k_{\mathrm{L,s}}$ (m s^{-1}) was described by the small-eddy model, which relies on the framework of surface renewal considering that the small eddies contribute to the renewal (Lamont and Scott, 1970; Moog and Jirka, 1999a). The model has been validated in a variety of environmental conditions, natural systems, and forcing mechanisms (Huang et al., 2022; Zappa et al., 2007) and could be expressed as:

$$k_{L,S} = \alpha Sc^{-1/2}(\varepsilon \nu)^{1/4} \tag{11}$$

In which the rate of dissipation of turbulent kinetic energy (ε) is evaluated at the surface, where the leading factor α = 0.18logε + 0.90 (Wang et al., 2015). The surface dissipation rates in this study were determined through numerical simulations (the details of the numerical modeling refer to Appendix. C). Fig. 10a and 10b depict the evolution in dissipation rates along the hydraulic jumps for two examples. In all cases, a sharp decrease in surface dissipation rate is observed along the initial half of the jump length, after which the surface dissipation rates stabilize at a consistently lower value (Fig. 10c). The surface energy dissipation rate profiles align with pronounced oscillations near the jump toe and consistent wave propagations downstream. The profiles can be fitted by Equation 12 below (The goodness of fit R^2 = 0.92, examples of the fit in Fig. 10c), which in turn can be utilized for subsequent calculations of the small eddy model (Equation 11) along the surface of the hydraulic jump:

$$\frac{\varepsilon}{U_1^3/d_1} = \frac{1}{100}\left(C_1 \cdot \exp\left(-5\left(\frac{x-x_t}{L_j}\right)\right) + C_2\right) \tag{12}$$

Herein, C_1 and C_2 are parameters related to the inflow Froude number, which could be respectively described by the following equations:

$$C_1 = 11.4\exp(-(Fr_1 - 1)) + 0.18 \tag{13}$$

$$C_2 = \frac{0.15}{Fr_1 - 1} \tag{14}$$

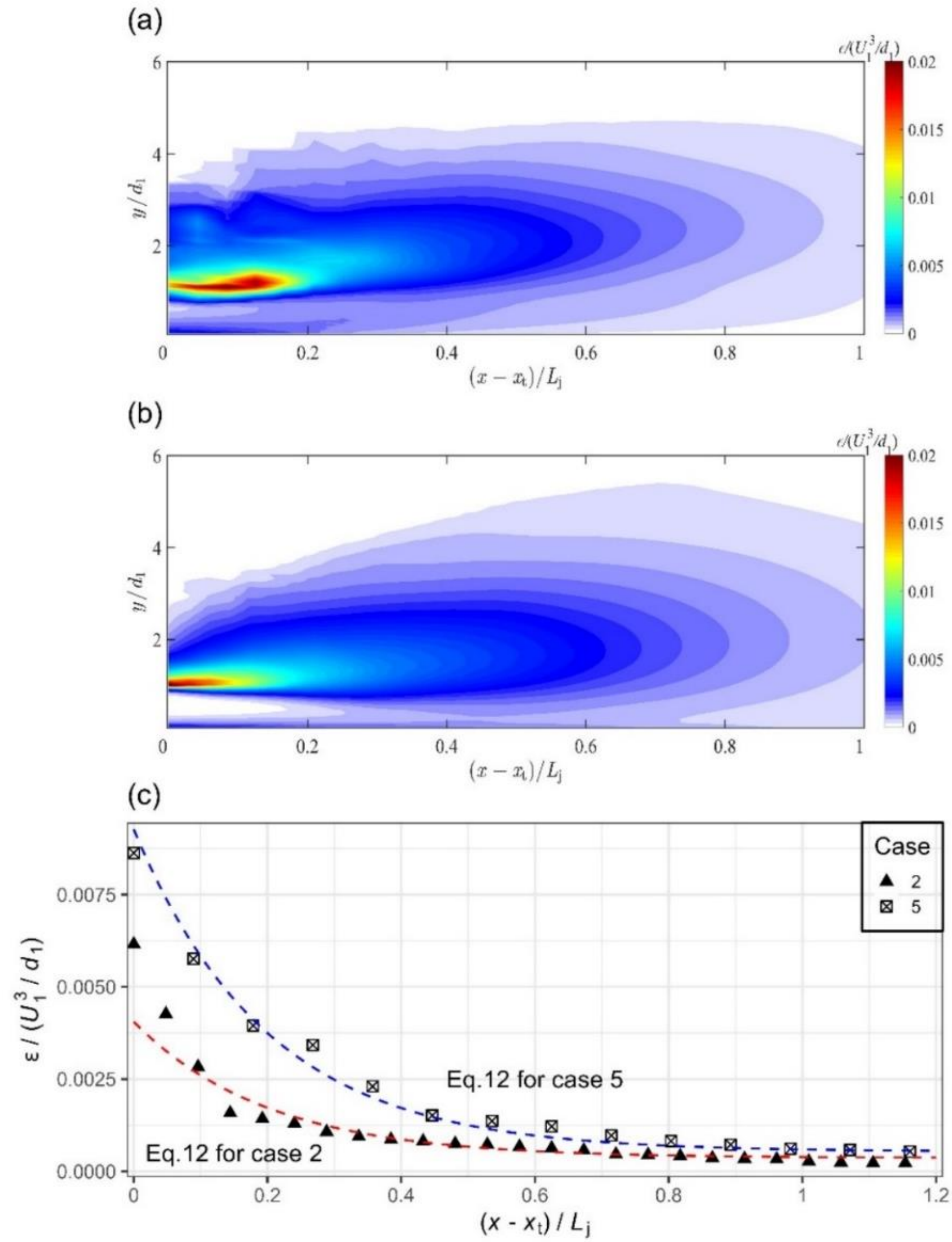

Fig. 10 Dimensionless dissipation rate of the turbulent kinetic energy for selected cases calculated by numerical simulations: (a) Case 5, Fr_1 = 2.98, $Re = 1.6 \times 10^5$; (b) Case 2, Fr_1 = 5.57, $Re = 1.4 \times 10^5$; (c) free surface dissipation rates along the hydraulic jumps

The active interfacial areas A(x) along the hydraulic jump were estimated based on the surface profile of the hydraulic jump and the channel width w. Fig. 11 presents the geometry of the time-averaged free surface of the hydraulic jumps. The profile follows:

$$\frac{y-d_1}{d_2-d_1}=\left(\frac{x-x_t}{L_j}\right)^{C_p}, \quad 0 \le x-x_t \le L_j \tag{15}$$

where d_1 and d_2 are the upstream and downstream conjugate depths, and C_p is a constant, determined as 0.638 in our study.

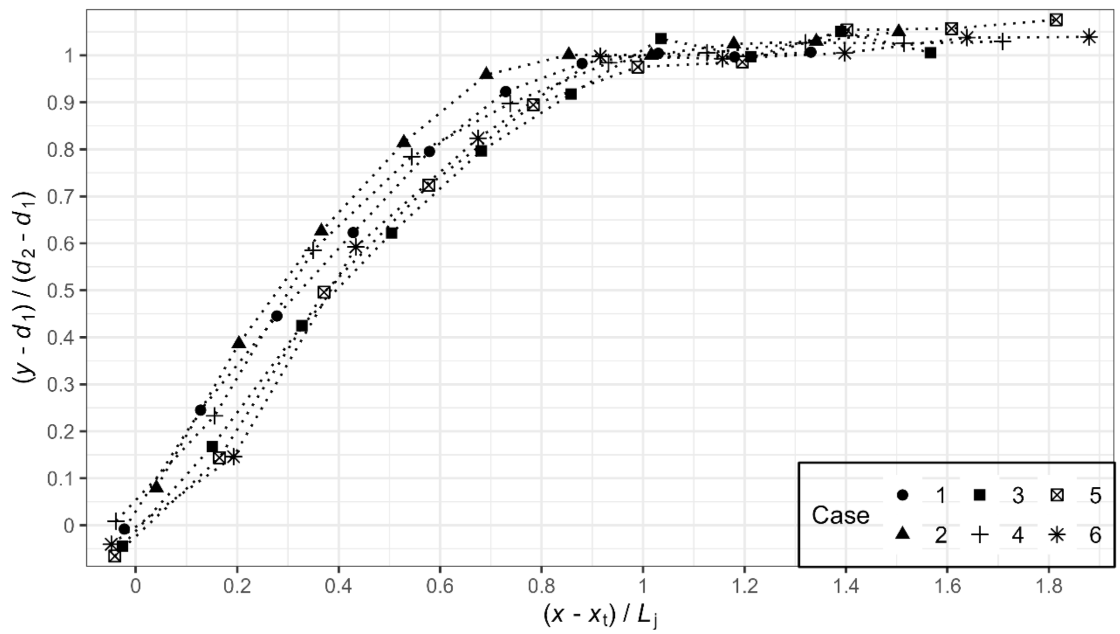

Fig. 11 Dimensionless time-averaged water elevation profiles for all cases of hydraulic jumps

The volumetric free surface contribution $(k_L a)_s$ could be simplified as:

$$(k_L a)_s = \int_0^{L_j} k_{L,s}(x)\frac{dA(x)}{V_j} = \frac{w}{V_j}\int_0^{L_j} k_{L,s}(x)\sqrt{1+y'^2}\,dx \qquad (16)$$

Where V_j represents the volume of the hydraulic jump and $y' = dy/dx$, where y is described by Equation 15. Figure 12 illustrates the correlation between volumetric free surface contribution, $(k_L a)_s$, and the inflow Froude number. Notably, as the inflow Froude number increases, the free surface contribution remains relatively constant at around 1000 day^{-1}. While higher rates of surface energy dissipation and gas transfer velocities are observed, particularly near the jump toe in more intense hydraulic jumps (with a higher inflow Froude number), these cases also exhibit longer hydraulic jump lengths and larger volumes. Ultimately, this results in relatively comparable volumetric transfer contributions. It is important to note that the calculation method, which involves taking the time-averaged profile, overlooks the fluctuation characteristics of the free surface. This may lead to an underestimation of volumetric gas transfer contributions, and this underestimation is likely to become more pronounced for more intense hydraulic jumps. In the gas transfer model validation section, the potential underestimation is further elaborated.

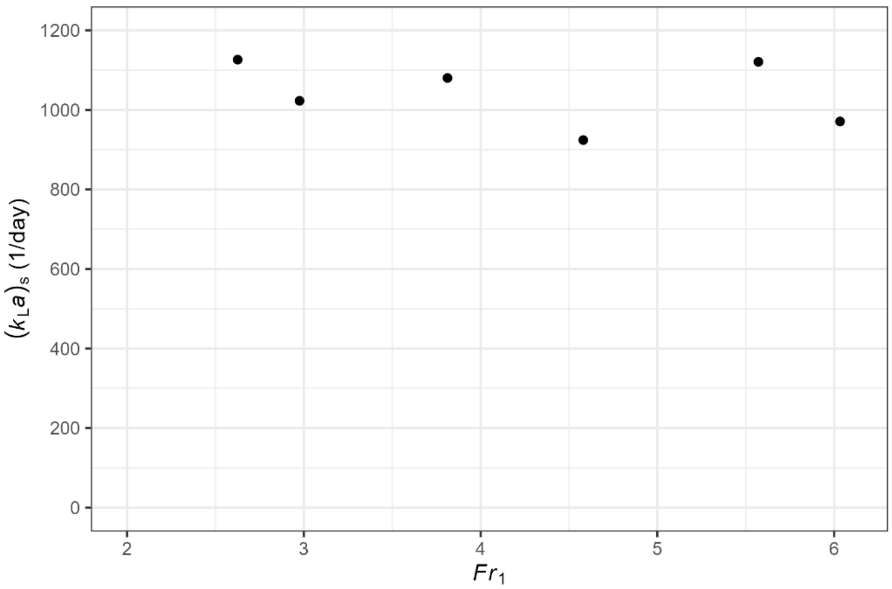

Fig. 12 Free-surface gas transfer contribution for hydraulic jumps

Bubble-Mediated Pathway Contribution

The singular air entrainment at the jump toe is a major feature differing from interfacial air-water exchange processes. The interaction between bubbles and internal turbulent flow is intense, leading to bubble breakup, coalescence and complex transport and recirculation. Using the dual-tip conductivity probe, the bubble characteristics were investigated. As an example, Fig. 13a and 13b show the typical void fraction and bubble count rate profiles at three cross sections along a tested hydraulic jump (Case 2). The profiles reveal two distinct flow regions: the turbulent shear region and the recirculation region. In the turbulent shear region, the time-averaged void fraction forms a bell-shaped profile from zero at the channel bed to a characteristic elevation with a local minimum. The bubble count rate sharply increases from zero to a maximum with increasing elevation from the bed, and, for larger elevations, there is a reduction of the bubble count rate to a local minimum at the upper boundary of the turbulent shear region. The recirculation region comprises a bubbly flow region below and a splashing free-surface area above the mean water elevation. The void fraction gradually increases to unity across the recirculation region, while the bubble count rate shows a secondary peak and then decreases to zero above the roller surface. These characteristics of bubbles pose challenges in accurately estimating the bubble-mediated path contribution.

The behavior of bubble transfer velocity of small bubbles $k_{L,b}^{S}$ and large bubbles $k_{L,b}^{L}$ are different due to divergent interfacial dynamics. Kawase and Moo-Young (1992) characterized these transfer velocities by the following equations, and the equations have been successfully applied and validated by Toombes and Chanson (2005) and Felder and Chanson (2014) in the context of stepped chutes:

$$\begin{cases} k_{L,b}^{S} = 0.28 Sc^{-2/3} \upsilon^{1/3} g^{1/3} & d_b < 2.5 \text{ mm} \\ k_{L,b}^{L} = 0.47 Sc^{-1/2} \upsilon^{1/3} g^{1/3} & d_b \geq 2.5 \text{ mm} \end{cases} \tag{17}$$

where d_b is the representative bubble diameter. The complex flow regime of hydraulic jump results in a mix of small and large bubbles across most regions, and for simplicity, the sectional average transfer velocity $k_{L,b}$ could be expressed as a combination of bubble transfer velocity from bubbles of different sizes:

$$k_{L,b} = \phi k_{L,b}^{S} + (1-\phi) k_{L,b}^{L} \tag{18}$$

where ϕ is the proportion of the number of small bubbles in the total bubbles at each measuring location, determined by:

$$\phi = \frac{1}{Y_{90}} \int_{0}^{Y_{90}} \frac{N_b^S(y)}{N_b^S(y) + N_b^L(y)} \cdot dy \tag{19}$$

where N_b^S is the number of small bubbles (d_b < 2.5 mm) while N_b^L is the number of big bubbles ($d_b \geq$ 2.5 mm), Y_{90} is the characteristic flow depth where C = 0.9. During each sampling experiment, the chord length of every passing-by bubble could be detected and categorized into small or big bubble groups, and the whole number and small bubble proportion could further be obtained. The cross-sectional proportions of small bubbles ϕ were presented in Fig. 14. The graph indicates a progressive rise in the ratio of small bubbles from the jump toe, reaching its peak between around 0.4 L_j to 0.6 L_j. This signifies a noticeable trend of breakup resulting from internal interactions. Subsequently, the ratio experiences a decline.

In a hydraulic jump, the specific interfacial area for bubbles (a_b) at each flow depth is estimated to be proportional to the number of air-water interfaces per unit length of air-water mixture (Chanson, 1997; Toombes and Chanson, 2005):

$$a_b = n \frac{2F}{U_b} \tag{20}$$

where n is a constant representing the shape of the bubbles, and it usually takes a value of 2 in the hydraulic jump. F is the bubble count rate defined as the number of bubbles passed by the sensor needle per second, U_b is the air-water interfacial velocity, calculated as the distance between neighboring needle tips over the time interval of a bubble reaching the needles. The dimensionless bubble count rate and air-water interfacial velocity for a tested hydraulic jump (case 2) at three cross sections were presented in Fig. 13b, 13c, and 13d.

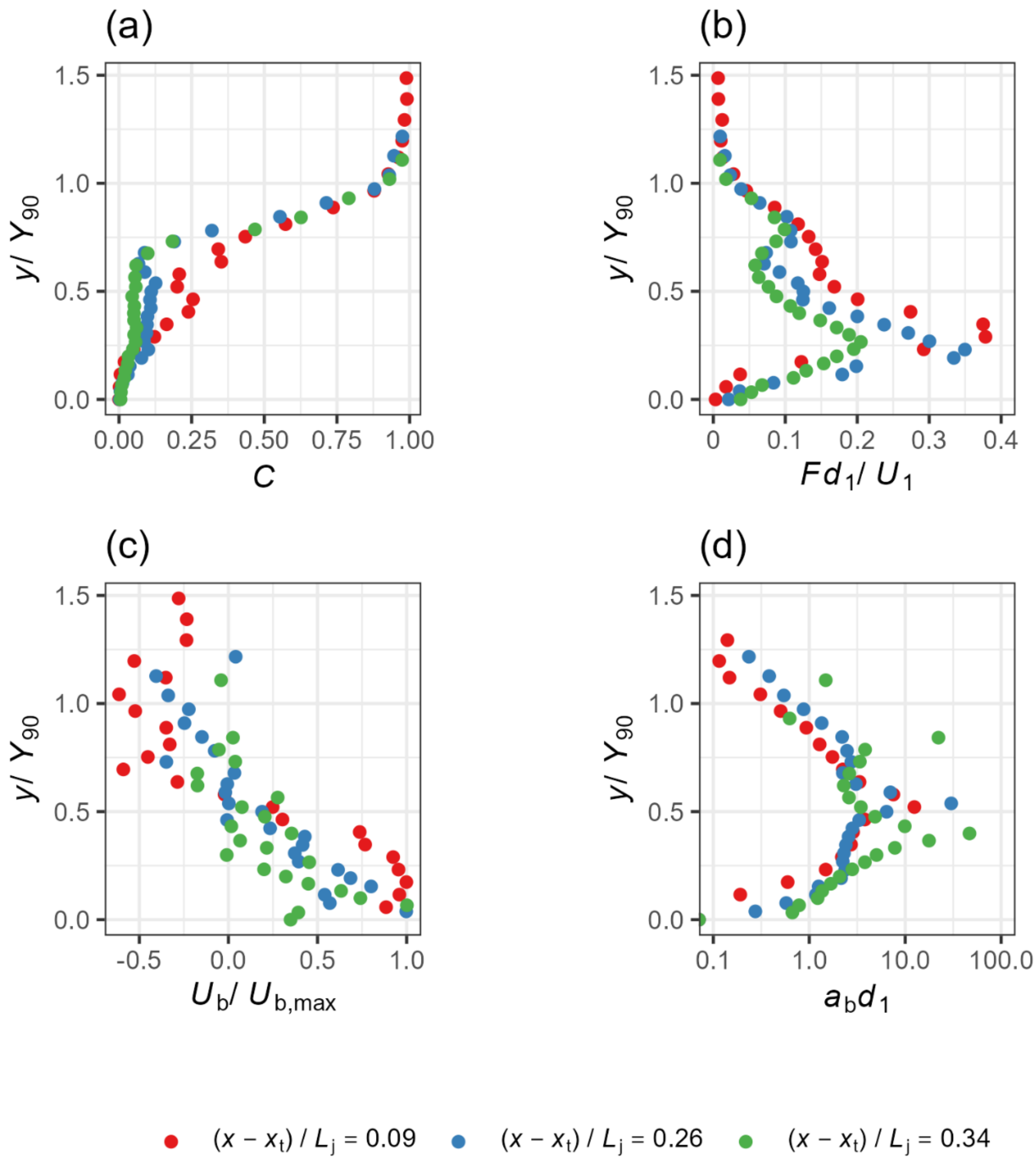

Fig. 13 Typical air-water flow characteristics of case 2 at three cross sections, for (a) void fraction distribution; (b) dimensionless bubble count rate distribution; (c) dimensionless air-water velocity distribution; (d) dimensionless specific interfacial area for bubbles

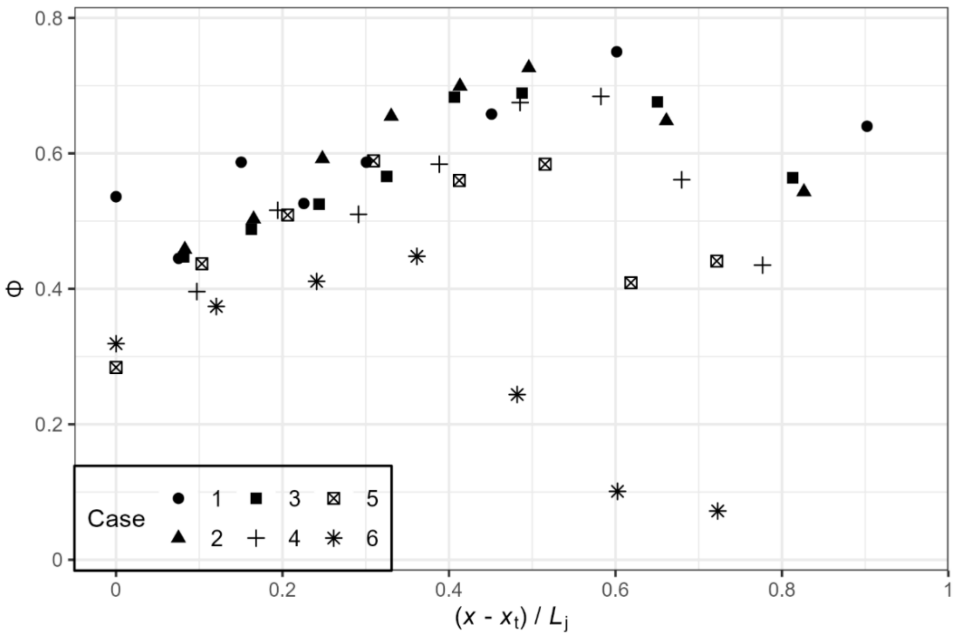

Fig.14 Cross-sectional averaged proportion of small bubbles along the hydraulic jumps

The volumetric bubble-mediated contribution $(k_L a)_b$ within the hydraulic jump is governed by the bubble transfer velocity $k_{L,b}$ and specific interfacial area for the bubble a_b:

$$(k_L a)_b = \frac{1}{L_j}\int_0^{L_j} k_{L,b}(x) a_{b,mean}(x) dx \tag{21}$$

where the sectional average specific interfacial area for bubbles $a_{b,mean}$ could be calculated by:

$$a_{b,mean}(x) = \frac{1}{Y_{90}}\int_0^{Y_{90}} a_b(x,y) dy \tag{22}$$

A more pronounced hydraulic jump gets more bubbles entrained, and with intensified internal interplay, large bubbles are more susceptible to break up, thus water-air contacting areas are greatly enlarged. Besides, breakup induces a larger proportion of small bubbles. These small bubbles, marked by immobile surfaces, encounter friction drag, causing hindered flow within the boundary layer (Calderbank and Moo-Young, 1961), thereby boosting the bubble-mediated gas transfer velocity. The cumulative impact of these effects significantly amplifies the overall contribution of bubble-mediated transfer. The results were illustrated in Fig. 15.

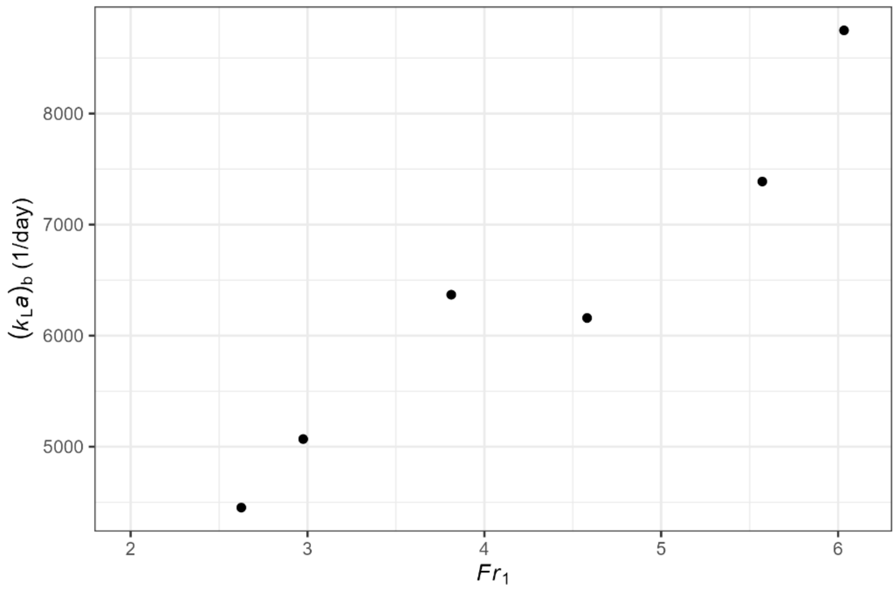

Fig. 15 Bubble-mediated gas transfer contribution for hydraulic jumps

Gas Transfer Model Validation

The primary pathways for gas transfer between air and water involve contributions from the free surface and bubble-mediated processes. In Fig. 16, we compare the combined effects of these two components (as calculated by the modeling approach devised in the previous sections) against values obtained from channel experiments. Notably, our model produces generally good results without the inclusion of any calibrated coefficients. However, it's important to highlight that the predicted outcomes from our model tend to be consistently smaller than the measured values, and this tendency becomes more pronounced with higher inflow Froude numbers.

Several factors contribute to this underestimation. For the free surface pathway, there is a potential underestimation of the active surface area for the free surface. The fluctuation characteristics along the hydraulic jump were presented in Fig. 17. It reveals significant fluctuations that enhance the air-water contact area. Filtering out these fluctuations by relying on the average profiles of the free surface resulted in an underestimation of active surface area. Further, dedicated studies are required to elucidate how significant this effect is, especially in light of the fact that, for most cases, $(k_L a)_s$ was estimated to be smaller than $(k_L a)_b$ (thus less important for the overall mass transfer). Besides, this model does not account for the additional gas transfer enhancement resulting from free surface behaviors, such as the rising and falling of droplets and large splashes, which have been overlooked.

For the bubble-mediated pathway, firstly the inability to capture microbubbles could lead to an underestimation of the bubble-mediated contribution as electrode diameter, flow rate, and sampling frequency collectively influence the maximum measurable bubble size. Microbubbles could both elevate the gas transfer velocity $k_{L,b}$ and specific area a_b. Secondly, the paired empirical equations of the bubble transfer velocity (equation 18) were derived in bubble column reactors where the liquid circulation is induced by primarily the buoyancy force. The equations would underestimate $k_{L,b}$ in hydraulic jumps since roller-wave flow structures induce extra turbulence. Thirdly, the assumption of a constant shape factor (n) as 2 when calculating the specific area for bubble a_b might contribute to the underestimation. This assumption is rooted in the concept of spherical and ellipsoidal bubbles, which may not universally apply across all sections and warrants further investigation. Fourthly, the impact of bubble residence time in water has not been fully considered. Bubbles that persist downstream and those rapidly exiting the water body exhibit distinct mass transfer performances.

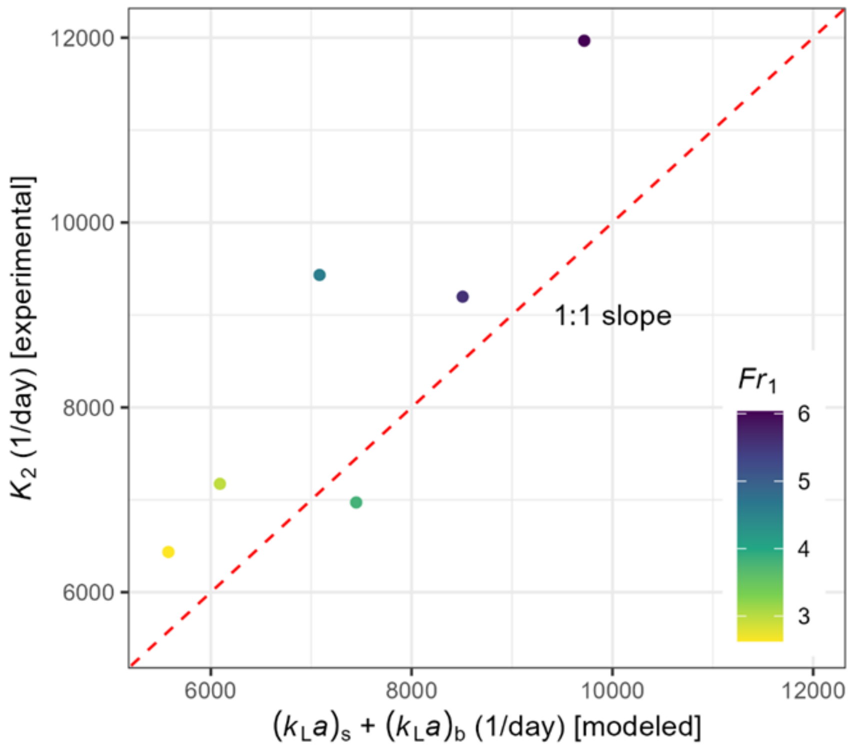

Fig. 16 Mechanistic gas transfer model validations using channel experiment data in this study

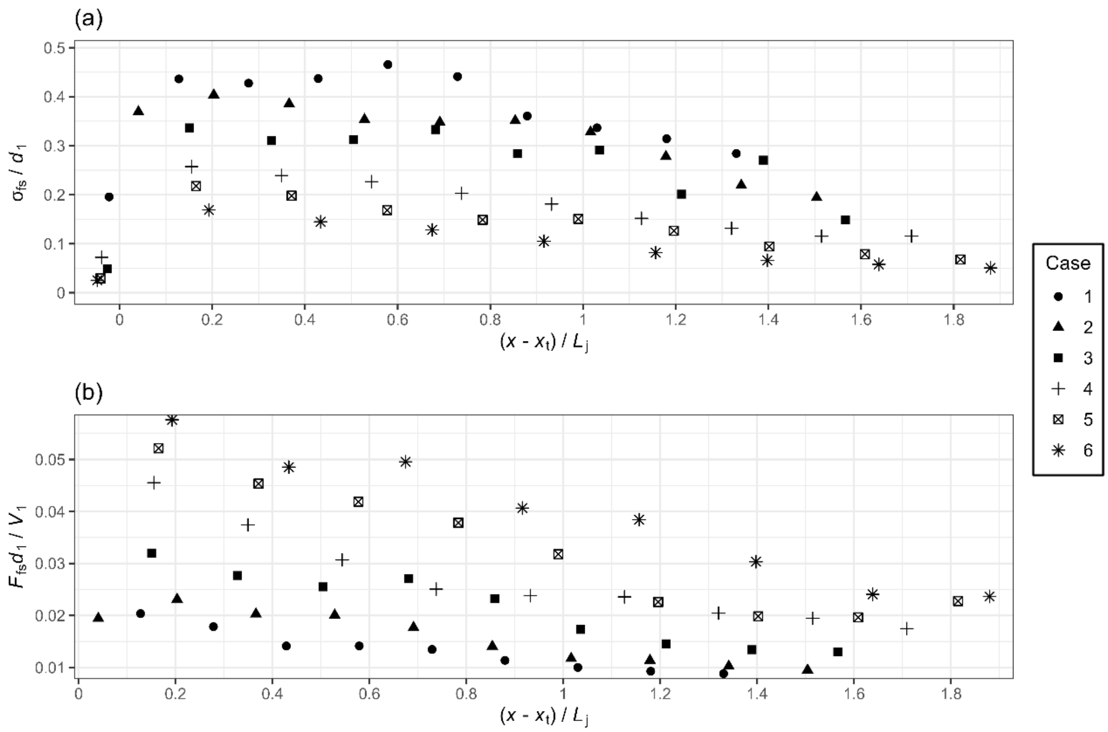

Fig. 17 Free surface fluctuation characteristics along the hydraulic jump (a) dimensionless free surface standard deviation; (b) dimensionless free surface fluctuation frequency

5. Discussion

5.1 Gas Transfer Heterogeneity

Gas transfer process presents a very strong heterogeneity in different flow regimes, which hinders regional or global exchange estimates. According to the summary of Hall et al. (2012), the mean gas transfer velocities normalized to a Schmidt number of 600 (k_{600}) vary between 0.8 to 5.8 m/day for estuaries, between 1.4 to 9.6 m/day for lowland rivers, but 336 m/day and with a maximum of 1855 m/day for Colorado rapids. Based on the Schmidt scaling law, we could transform our overall gas transfer velocity into a comparative metric (Jähne et al., 1987; Wanninkhof, 1992):

$$k_{600} = k_L \cdot (600 / Sc_{O2})^{-1/2} \quad (23)$$

where Sc_{O2} is the Schmidt number of oxygen, $Sc_{O2} = \nu/D_m$, with D_m the molecular diffusivity of oxygen in water. D_m is calculated using the Stokes-Einstein relationship and experimental data by St-Denis and Fell (1971). It is noteworthy that bubble-mediated gas transfer velocity will depend on both the solubility and diffusivity of the target gas, and simple scaling among gases by the ratio of the Schmidt numbers may cause many uncertainties (Asher and Wanninkhof, 1998; Asher et al., 1997).

In our channel experiments, the k_{600} values range from 340 to 985 m/day. These values closely align with the gas transfer velocity observed in rapid sections, underscoring the significance of bubble-mediated gas transfer. Additionally, considering flow self-adjustment and stability, events like hydraulic jumps or other substantial energy dissipation occurrences are highly localized. In simpler terms, overlooking any such event may lead to an underestimation of gas transfer. Conversely, applying a peak transfer velocity across an entire river range may result in an overestimation. To accurately estimate gas transfer in large-scale, high-energy flows, a more detailed flow characterization is imperative.

5.2 Free-Surface Transfer versus Bubble-Mediated Transfer

This paper distinguishes between free-surface transfer and bubble-mediated transfer in a typical self-aeration scenario. In Fig. 17, the proportion of contribution from these two components is illustrated. It is evident from the figure that the bubble-mediated part constitutes a larger proportion, particularly in cases with stronger hydraulic jumps and more intense air entrainment.

Moreover, in cases of relatively moderate bubble entrainment, such as case 6 in our experiments with Fr_1 = 2.63 (commonly occurring in canals), the ratio of free-surface contribution to bubble-mediated contribution is 1:4. Disregarding the contribution from the free surface could result in an underestimation. While scaling free-surface gas transfer is relatively straightforward, bubble clouds introduce complexity. Bubble-mediated gas transfer heavily depends on bubble size distribution and bubble transport laws. Given the evident scale effects in related bubble characteristics, caution is warranted when extrapolating from scaled-down indoor experiments. Additionally, mechanics related to bubble entrainment will also impact the results. To be more specific, self-aeration caused by surface deformation and strong turbulence may not follow a similar gas transfer law as artificially induced homogeneous plumes with well-separated bubbles (Klaus et al., 2022).

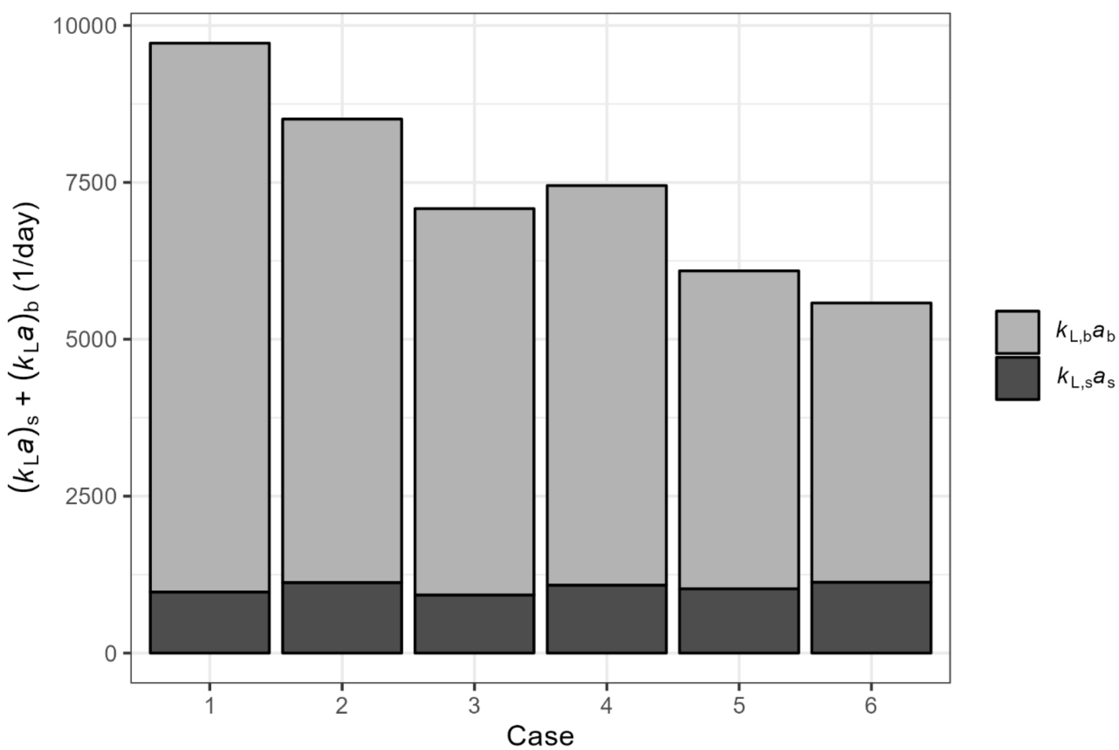

Fig. 17 Gas transfer comparison between calculated free-surface contribution and calculated bubble-mediated contribution

6. Conclusions

The gas transfer process for hydraulic jumps was investigated in a recirculating flume for $2.63 < Fr_1 < 6.03$ and $1.32 \times 10^5 < \mathrm{Re} < 1.62 \times 10^5$. The gas transfer efficiency E across the hydraulic jump lies between 0.037 to 0.162. These values are 4 to 7 times larger than those reported in previous comparable studies, highlighting the substantial impact of scale effects in bubble dynamics on gas transfer. The local gas transfer velocities, normalized to a Schmidt of 600 (k_{600}) exhibit a range from 340 to 985 m/day. These values are two orders of magnitude greater than those for estuaries and lowland rivers but are comparable to rapids in a large whitewater river.

Based on the detailed measurements and numerical simulations, we explicitly resolve the dynamics of both free-surface and bubbles. Subsequently, we developed a mechanistic volumetric gas transfer model tailored for the highly agitated running flows by establishing the relationships between the gas transfer law and hydrodynamics in two-phase flows. The model aligned well with our experimental data and was capable of physically clarifying the gas transfer contribution from free-surface parts and bubble-mediated parts. To a certain extent, the results elucidate the reasons for gas transfer heterogeneity for different flows and provide insights into gas transfer estimation on a large scale.

Appendix A. Gas Transfer Efficiency Calculation in the Recirculation System

The water in the system is assumed to be thoroughly mixed, and the bulk dissolved oxygen (DO) concentration, denoted as $C(t)$, remains uniform throughout the system at all times during the experiments. The total water volume within the system, denoted as V_{sys}, encompasses the water of both the head and tail tanks, as well as the content within the flume and recirculation pipe.

The total input of gas molecules to the water in the system ($\dot{m}$) consists of the sum of the transfer through the hydraulic jump ($\dot{m}_j$) and the background reaeration ($\dot{m}_0$). These can be written in terms of transfer coefficients as:

$$\dot{m} = K_{vol}[C_S - C(t)]V_{sys} \tag{A1}$$

$$\dot{m}_j = K_{vol}^j[C_S - C(t)]V_{sys} \tag{A2}$$

$$\dot{m}_0 = K_{vol}^0[C_S - C(t)]V_{sys} \tag{A3}$$

where K_{vol}^j and K_{vol}^0 represent volumetric transfer coefficients corresponding to the jump reaeration rates and background reaeration rates for the whole system respectively; K_{vol} is an equivalent volumetric transfer coefficient for the whole system. Considering well-mixed water and constant V_{sys}, the DO mass balance for the system can be expressed as:

$$\frac{d[C(t)V_{sys}]}{dt} = K_{vol}[C_S - C(t)]V_{sys} \Rightarrow \frac{dC(t)}{dt} = K_{vol}[C_S - C(t)] \tag{A4}$$

The volumetric transfer coefficient for the hydraulic jump K_2^j could be derived by:

$$K_2^j = K_{vol}^j \frac{V_{sys}}{V_j} = (K_{vol} - K_{vol}^0)\frac{V_{sys}}{V_j} \tag{A5}$$

where V_j is the volume of the hydraulic jump.

The gas transfer efficiency of the hydraulic jump could be calculated by:

$$E = \frac{C_d - C_u}{C_S - C_u} = 1 - e^{-K_2^j t} \quad \text{(A6)}$$

where C_u and C_d are the DO concentrations at the upstream and downstream of the hydraulic jump, respectively. t is the average travel time of water between the upstream and downstream ends of the control volume $t = V_j/Q$. E has a range between 0, for no oxygen transfer and 1, for total downstream saturation. It could be further derived:

$$E = 1 - e^{-(K_{vol} - K_{vol}^0)\frac{V_{sys}}{V_j}\frac{V_j}{Q}} = 1 - e^{-(K_{vol} - K_{vol}^0)\frac{V_{sys}}{Q}} \quad \text{(A7)}$$

Appendix B. Two Gas Transfer Pathways for Hydraulic Jump

For hydraulic jumps with obvious air entrainment, the gas transfer encompasses a free surface pathway and a bubble-mediated pathway, the mass balance equation for the hydraulic jump could be furtherly expressed as:

$$\frac{dC(t)}{dt} = (k_L a)_s (C_S - C(t)) + (k_L a)_b (C_{eff} - C(t)) \quad \text{(B1)}$$

where $(k_L a)_s$ and $(k_L a)_b$ denote the volumetric contribution for free surface and bubble respectively. C_{eff} means effective saturation concentration at the bubble–water interface at some depth, and C_{eff} could be taken as C_S in our study since the impact of water depth in our experiments is negligible. It could be furtherly derived:

$$K_2^j = (k_L a)_s + (k_L a)_b \quad \text{(B2)}$$

Appendix C. Numerical Modelling

The surface dissipation rate of the turbulent kinetic energy is an important parameter to scale the surface turbulence and quantify the gas transfer. However, the dissipation rate in the highly agitated air-water two-phase flows like hydraulic jumps could be hardly measured with accuracy in an experimental way. Thus, the hydraulic jump in the flume was also numerically simulated to obtain a reasonable estimation of the turbulent dissipation rate values. The model solves the Reynolds-averaged Navier-Stokes (RANS) equations for the mean flows. The turbulence closure is accomplished by the k-ε two-equation model. The evolution of the free surface is modeled using the volume-of-fluid (VOF) method.

The two-dimensional computational domain was established based on the experimental section between the upstream nozzle and the downstream exit of the flume. For each simulation scenario, the height of the computational domain was sufficiently greater than the maximum flow depth. To simulate average mixed flow, the model enforced a no-slip boundary condition at the solid boundaries. To reduce computational complexity, turbulence development near the solid boundaries within the boundary layer was not explicitly resolved; instead, it was handled using wall functions. The computational domain was discretized into a uniform grid system with grid dimensions of 0.025 m × 0.003 m. The equivalent roughness was set to 0.15 mm, and the initial state of the fluid was at rest. Following established physical modeling practices, we simulated the flow until it reached a stable state, typically around 45 s, to ensure proper analysis of the hydraulic jump oscillations around its mean position. The detailed model configuration, mesh sensitivity analysis and model validation against physical data are not presented for the sake of conciseness, but similar model setup and treatment are reported in Wang et al. (2023).

Utilizing optical flow (OF) techniques, Wüthrich et al. (2021) estimated the dimensionless surface turbulence energy dissipation rate on breaking bores characterized by strong free-surface turbulence and significant air entrainment ($Fr_1 = 2.45$, $Re = 1.86 \times 10^5$). The magnitude and trend observed in their findings align closely with the outcomes derived from our numerical simulations. This convergence serves as additional evidence bolstering the credibility of our results.

Acknowledgments

The research is funded by the National Natural Science Foundation of China (52309101), Joint Funds of National Natural Science Foundation of China (U23A20668), China Postdoctoral Science Foundation (2023M732478), Sichuan Science and Technology Program (2023NSFSC0949), Research Fund of Sichuan University for Postdoctoral Researcher (2022SCU12128), Sichuan University Postdoctoral Interdisciplinary Innovation Fund (JCXK2209), and the Fundamental Research Funds for the Central Universities.

Open Research

Data Availability Statement

Supporting data used to create all figures in this paper can be accessed via the following link: https:// https://data.mendeley.com/datasets/v3bykvthr9/1, with the data set's https://doi.org/10.17632/v3bykvthr9.1.

References

Apted, R., and P. Novak (1973), Oxygen Uptake at Weirs, paper presented at Proceedings of the 15th Congress, IAHR Istanbul, Turkey.

Asher, W., and R. Wanninkhof (1998), Transient Tracers and Air-Sea Gas Transfer, Journal of Geophysical Research: Oceans, 103(C8), 15939-15958.

Asher, W. E., L. M. Karle, and B. J. Higgins (1997), On the Differences between Bubble-Mediated Air-Water Transfer in Freshwater and Seawater, Journal of Marine Research, 55(5).

Avery, S., and P. Novak (1975), Oxygen Uptake in Hydraulic Jumps and at Overfalls, paper presented at Proceedings of 16th IAHR Congress, Sao Paulo, Brazil.

Avery, S., and P. Novak (1978), Oxygen Transfer at Hydraulic Structures, Journal of the Hydraulics Division, 104(11), 1521-1540.

Bennett, J. P., and R. Rathbun (1971), Reaeration in Open-Channel Flow, US Government Printing Office.

Blaszczak, J. R., L. E. Koenig, F. H. Mejia, L. Gómez-Gener, C. L. Dutton, A. M. Carter, N. B. Grimm, J. W. Harvey, A. M. Helton, and M. J. Cohen (2023), Extent, Patterns, and Drivers of Hypoxia in the World's Streams and Rivers, Limnology and Oceanography Letters, 8(3), 453-463.

Botter, G., A. Carozzani, P. Peruzzo, and N. Durighetto (2022), Steps Dominate Gas Evasion from a Mountain Headwater Stream, Nature Communications, 13(1), 7803.

Bung, D. B., and D. Valero (2018), Re-Aeration on Stepped Spillways with Special Consideration of Entrained and Entrapped Air, Geosciences, 8(9), 333.

Calderbank, P. H., and M. B. Moo-Young (1961), The Continuous Phase Heat and Mass-Transfer Properties of Dispersions, Chemical Engineering Science, 16(1), 39-54.

Chan, W. C., and L. E. Scriven (1970), Absorption into Irrotational Stagnation Flow. A Case Study in Convective Diffusion Theory, Industrial & Engineering Chemistry Fundamentals, 9(1), 114-120.

Chanson, H. (1995), Air-Water Gas Transfer at Hydraulic Jump with Partially Developed Inflow, Water Research, 29(10), 2247-2254.

Chanson, H. (1997), Measuring Air-Water Interface Area in Supercritical Open Channel Flow, Water Research, 31(6), 1414-1420.

Chanson, H., and L. Toombes (2002), Air–Water Flows Down Stepped Chutes: Turbulence and Flow Structure Observations, International Journal of Multiphase Flow, 28(11), 1737-1761.

Danckwerts, P. V. (1951), Significance of Liquid-Film Coefficients in Gas Absorption, Industrial and Engineering Chemistry, 43(6), 1460-1467.

Felder, S., and H. Chanson (2014), Aeration and Air-Water Mass Transfer on Stepped Chutes with Embankment Dam Slopes, Environmental Fluid Mechanics, 15, 695-710.

Fortescue, G., and J. R. A. Pearson (1967), On Gas Absorption into a Turbulent Liquid, Chemical Engineering Science, 22, 1163-1176.

Gulliver, J., S., S. Wilhelms, C., and K. Parkhill, L. (1998), Predictive Capabilities in Oxygen Transfer at Hydraulic Structures, Journal of Hydraulic Engineering, 124(7), 664-671.

Hall, R. O., T. A. Kennedy, and E. J. Rosi-Marshall (2012), Air–Water Oxygen Exchange in a Large Whitewater River, Limnology and Oceanography, 2(1), 1-11.

Henderson, F. M. (1966), Open Channel Flow, MacMillan, New York.

Higbie, R. (1935), The Rate of Absorption of a Pure Gas into a Still Liquid During Short Periods of Exposure, Transactions of the American Institute of Chemical Engineers, 31, 365-389.

Holler, A. (1971), The Mechanism Describing Oxygen Transfer from the Atmosphere to Discharge through Hydraulic Structures, paper presented at Proc. 14th IAHR.

Huang, J., W. Zhao, Z. Li, Y. Ou, and L. Lin (2022), Estimation of Co2 Emission in Reservoir Coupling Floating Chamber and Thin Boundary Layer Methods, Science of The Total Environment, 811, 151438.

Jähne, B., G. Heinz, and W. Dietrich (1987), Measurement of the Diffusion Coefficients of Sparingly Soluble Gases in Water, Journal of Geophysical Research: Oceans, 92(C10), 10767-10776.

Kamal, R., D. Z. Zhu, J. A. Crossman, and A. Leake (2020), Case Study of Total Dissolved Gas Transfer and Degasification in a Prototype Ski-Jump Spillway, Journal of Hydraulic Engineering, 146(9).

Kawase, Y., and M. Moo-Young (1992), Correlations for Liquid-Phase Mass Transfer Coefficients in Bubble Column Reactors with Newtonian and Non-Newtonian Fluids, The Canadian Journal of Chemical Engineering, 70(1), 48-54.

Klaus, M., T. Labasque, G. Botter, N. Durighetto, and J. Schelker (2022), Unravelling the Contribution of Turbulence and Bubbles to Air-Water Gas Exchange in Running Waters, Journal of Geophysical Research: Biogeosciences, e2021JG006520.

Kucukali, S., and S. Cokgor (2006), Aeration Performance of a Hydraulic Jump, in World Environmental and Water Resource Congress 2006, edited, pp. 1-10.

Kucukali, S., and S. Cokgor (2020), An Experimental Investigation of Reaeration and Energy Dissipation in Hydraulic Jump, in Recent Trends in Environmental Hydraulics, edited, pp. 127-136, Springer.

Lamont, J. C., and D. S. Scott (1970), An Eddy Cell Model of Mass Transfer into the Surface of a Turbulent Liquid, AIChE Journal, 16(4), 513-519.

Lauerwald, R., G. G. Laruelle, J. Hartmann, P. Ciais, and P. A. G. Regnier (2015), Spatial Patterns in Co2 Evasion from the Global River Network, Global Biogeochemical Cycles, 29(5), 534-554.

Lewis, W. K., and W. G. Whitman (1924), Principles of Gas Absorption, Industrial & Engineering Chemistry, 16(12), 1215-1220.

McCready, M. J., E. Vassiliadou, and T. J. Hanratty (1986), Computer Simulation of Turbulent Mass Transfer at a Mobile Interface, AIChE Journal, 32(7), 1108-1115.

Moog, D. B., and G. H. Jirka (1999a), Air-Water Gas Transfer in Uniform Channel Flow, Journal of Hydraulic Engineering, 125(1), 3-10.

Moog, D. B., and G. H. Jirka (1999b), Stream Reaeration in Nonuniform Flow: Macroroughness Enhancement, Journal of Hydraulic Engineering, 125(1), 11-16.

Pearson, R. K. (1999), Data Cleaning for Dynamic Modeling and Control, 1999 European Control Conference (ECC), 2584-2589.

R. Core Team (2022), R: A Language and Environment for Statistical Computing, R Foundation for Statistical Computing, Vienna, Austria.

Raymond, P. A., et al. (2013), Global Carbon Dioxide Emissions from Inland Waters, Nature, 503(7476), 355-359.

St-Denis, C., and C. Fell (1971), Diffusivity of Oxygen in Water, The Canadian Journal of Chemical Engineering, 49(6), 885-885.

Tamburrino, A., and J. S. Gulliver (2002), Free-Surface Turbulence and Mass Transfer in a Channel Flow, AIChE Journal, 48(12), 2732-2743.

Toombes, L., and H. Chanson (2005), Air–Water Mass Transfer on a Stepped Waterway, Journal of Environmental Engineering, 131(10), 1377-1386.

Ulseth, A. J., R. O. Hall, M. Boix Canadell, H. L. Madinger, A. Niayifar, and T. J. Battin (2019), Distinct Air–Water Gas Exchange Regimes in Low- and High-Energy Streams, Nature Geoscience, 12(4), 259-263.

Valero, D. (2018), On the Fluid Mechanics of Self-Aeration in Open Channel Flows, Ph.D. thesis thesis, Université de Liegé, Liegé, Belgique.

Vautier, C., R. Abhervé, T. Labasque, A. M. Laverman, A. Guillou, E. Chatton, P. Dupont, L. Aquilina, and J.-R. de Dreuzy (2020), Mapping Gas Exchanges in Headwater Streams with Membrane Inlet Mass Spectrometry, Journal of Hydrology, 581, 124398.

Wang, B., Q. Liao, J. H. Fillingham, and H. A. Bootsma (2015), On the Coefficients of Small Eddy and Surface Divergence Models for the Air-Water Gas Transfer Velocity, Journal of Geophysical Research: Oceans, 120(3), 2129-2146.

Wang, H., C. Ni, W. Lyu, and L. Tang (2023), A-Type Hydraulic Jumps over a Negative Step: Numerical Investigation Based on Composite Modeling and Validation, Physics of Fluids, 35(10).

Wanninkhof, R. (1992), Relationship between Wind-Speed and Gas-Exchange over the Ocean, Journal of Geophysical Research-Oceans, 97(C5), 7373-7382.

Wilhelms, S. C., L. Clark, J. R. Wallace, and D. R. Smith (1981), Gas Transfer in Hydraulic JumpsRep. E-81-10, Georgia institution of technique Atlanta school of civil engineering

Wüthrich, D., R. Shi, and H. Chanson (2021), Strong Free-Surface Turbulence in Breaking Bores: A Physical Study on the Free-Surface Dynamics and Air–Water Interfacial Features, Journal of Fluid Mechanics, 924, A20.

Zappa, C. J., W. R. McGillis, P. A. Raymond, J. B. Edson, E. J. Hintsa, H. J. Zemmelink, J. W. H. Dacey, and D. T. Ho (2007), Environmental Turbulent Mixing Controls on Air-Water Gas Exchange in Marine and Aquatic Systems, Geophysical Research Letters, 34(10).

Zhao, W., A. Prata, W. Peirson, R. Stuetz, and S. Felder (2022), Reaeration in Supercritical Open Channel Flows: An Experimental Study, Journal of Hydraulic Engineering, 148(10), 04022016.

Zhao, W., W. Xu, H. Wang, R. Tang, and R. Bai (2024), Roller Fluctuations of Pre-Aerated High-Froude-Number Hydraulic Jumps, Proceedings of the Institution of Civil Engineers - Water Management, 177(1), 28-43.